

Flame propagation in aeronautical swirled multi-burners: Experimental and numerical investigation

David Barré^{a,*}, Lucas Esclapez^a, Matthieu Cordier^b, Eleonore Riber^a, Bénédicte Cuenot^a, Gabriel Staffelbach^a, Bruno Renou^b, Alexis Vandel^b, Laurent Y.M. Gicquel^a, Gilles Cabot^b

^a CERFACS, 42 avenue G. Coriolis, 31 057 Toulouse Cedex 01, France

^b CORIA-UMR6614, Université et INSA de Rouen, 76 801 Saint-Etienne du Rouvray cedex, France

ARTICLE INFO

Article history:

Received 25 September 2013

Received in revised form 28 January 2014

Accepted 15 February 2014

Available online xxxx

Keywords:

Large Eddy Simulation

Ignition

Turbulent partially premixed flame

Flame propagation

Multi-injectors

ABSTRACT

Driven by pollutant emissions stringent regulations, engines manufacturers tend to reduce the number of injectors and rely on lean combustion which impacts the light-around phase of ignition. To improve knowledge of the ignition process occurring in real engines, current research combines fundamental and increasingly complex experiments with high fidelity numerical simulations. This work investigates the flame propagation, using a multi-injector experiment located at CORIA (France) in combination with Large Eddy Simulation (LES) obtained by CERFACS (France). The comparison of numerical fully transient ignition sequences with experimental data shows that LES recovers features found in the experiment. Global events such as the propagation of the flame front to neighboring swirlers are well captured by LES, with the correct propagation mode (spanwise or axial) and the correct overall ignition time delay. The detailed analysis of LES data allows to identify the driving mechanisms leading to each propagation mode.

© 2014 The Combustion Institute. Published by Elsevier Inc. All rights reserved.

1. Introduction

Pollutant emission reduction is currently one of the major constraints for the design of the next generation combustion chamber. It implies fuel consumption reduction and combustion efficiency increase. Very lean overall equivalent ratios are often used to reach pollutant emission targets. However very lean combustion is more subject to combustion instabilities and blow-off might happen at ground level or at high altitude. At the same time, to reduce the cost and weight of the combustor, designers intend to minimize the number of injection systems. For a given combustion chamber geometry, this solution implies a larger distance between consecutive injectors. Both lean combustion and fewer injectors raise concerns about a possible impact on relight performances, a major safety issue. It must then be ensured during the design phase that the distance between injectors always enables rapid and safe flame propagation in the combustion chamber during ignition.

The ignition process of a combustion chamber may be described in various successive steps [1]. Ignition is triggered by the deposition of energy from a spark plug or a laser beam, creating a plasma with very high pressure and temperature in a small volume around

the igniter [2]. This is also the location of the first chemical reactions. Then if the deposited energy is sufficient, chain branching reactions occur and lead to the formation of a small but expanding flame kernel. If the mixture and temperature conditions allow this kernel to reach a critical volume [3], it then generates a turbulent flame that is able to propagate upstream and ignite the first injector, and subsequently to propagate to the neighboring injectors. In very lean regimes and with the aim of reducing the number of fuel injectors, this last step could be problematic. To comply with safety regulations, it is crucial that the combustion chamber geometry enables flame propagation from one injector to another, ensuring full relight in a short time. This mechanism is very little addressed in the literature due to the high cost of multi-burner experiments and numerical simulations.

Numerous questions are often raised concerning the location of the spark and the minimum amount of energy to be deposited. Conventional wall igniters are far from being optimum, due to the unfavorable thermodynamic conditions at the walls. The amount of deposited energy is a compromise between the created flame kernel size and the spark plug reliability, considering that high levels of energy induce rapid erosion of the electrodes. Different studies on simple configurations [4–7] have shown the stochastic behavior of ignition and scenarios have been proposed based on local flow conditions and time history of the flame kernel.

* Corresponding author. Fax: +33 561193000.

E-mail addresses: barre@cerfacs.fr, david.barre33@gmail.com (D. Barré).

Following these fundamental studies, it is now accepted that ignition must be characterized with a statistical approach [6]. From a numerical point of view, this stochastic aspect is a major difficulty, because ignition probability can only be built from large samples i.e. high number of calculations, inducing a high computational cost and a lengthy process. To overcome this difficulty, predictive methodologies have been recently developed, involving only one cold flow Large Eddy Simulation (LES), and using local conditions [8] or flame kernel history [9] or RANS. This type of simple approach enables to rapidly evaluate the probability of the first steps of ignition in a sector of an annular combustion chamber. For the subsequent light-around phase, numerical simulation has shown to be an interesting path as evidenced by the pioneering work of Boileau et al. [10] that has given the first insights on the leading mechanisms of ignition in a fully annular complex geometries. The flame was found to be driven by the burnt gas expansion as it propagates mainly in the azimuthal direction at a speed much higher than the turbulent flame propagation velocity. More recently, Jones and Tyliszczak [11] investigated the ignition sequence of a realistic gas turbine sector, where the influence of the deposited energy on the overall ignition time was highlighted. These studies demonstrated that LES is a useful and necessary tool to investigate the last steps of ignition related to the flame stabilization and propagation in the whole burner.

Recently two research teams have started to investigate the light-around problem experimentally. Both experiments [12,13] studied pure premixed gaseous flow in simplified geometries while keeping major realistic burner features, namely an annular chamber with swirl stabilized injection systems. Bach et al. [12] studied the ignition sequence of a methane/air annular burner composed of 18 swirled injection systems. Keeping the global equivalence ratio constant at 0.7, the bulk flow velocity was found to have a detrimental effect on the overall ignition delay. This study also showed that to propagate from one burner to another, the flame has to be captured by the top of the inner recirculation zone. They also observed that flame propagation is promoted by swirl motion. Bourguin et al. [13] focused on a propane/air annular burner fitted with 16 swirled injectors. In agreement with the conclusions of Boileau et al. [10], the investigation showed the major role of the gas volumetric expansion on the flame propagation velocity. They also reported that for a constant global equivalence ratio of 0.76, the overall ignition time reduces with increasing bulk velocity which is in contradiction with the result of Bach et al. [12]. This highlights the complexity of the involved phenomena and the need for further studies.

In this context, the objective of the present study is to investigate the effect of the distance between injectors on the ignition light-around process using both experimental measurements and LES. The direct comparison of experiments and simulations in the propagative phase of an ignition sequence brings new insights on

the involved mechanisms. First LES of the experiment is performed under cold conditions to validate the approach by quantitative comparisons with measurements, as a prerequisite before studying ignition. LES of ignition sequences are then confronted to experiments in terms of propagation dynamics to verify the consistency of both approaches. Analysis is then conducted in an attempt to provide further understanding of the ignition transients.

2. Experimental and numerical setup

2.1. Experimental setup

2.1.1. Experimental burners description

To study ignition and subsequently the flame propagation process, a straight experimental setup initially composed by a maximum of 5 swirled injectors (Fig. 1) was designed by CORIA in the context of the European project KIAI (Knowledge for Ignition, Acoustics and Instabilities – 7th Framework Program – 2009/2013). The particularity of the test facility is that spacers can be introduced between consecutive injectors to evaluate the impact of the distance between injectors on the flame propagation and the overall time duration of the burner ignition phase. This distance can be gradually increased from 90 mm (without spacer) to 260 mm as seen in Fig. 2. A numbering convention regarding injectors from left to right as illustrated in Fig. 2 is adopted hereafter. It is composed of a central and an annular injection system. For the experiment, a large optical access allows an entire view of the combustion chamber (Fig. 1). Small optical accesses are located on transversal sides, enabling the use of optical diagnostics. The back of the combustion chamber is composed of a metallic plate of height 270 mm. The combustion chamber is ended with a convergent (top part of Fig. 1) having an adaptive length and a height of 200 mm, to prevent unwanted entry of air. The main axial length of the burner is referred as the Z-axis which also coincides with the main flow direction. The X and Y-axes respectively referred to as spanwise and cross-stream coordinates in a cartesian frame relative to the whole configuration. Note that with this definition, the spanwise direction coincides with the alignment direction of all burners. The cross-stream direction is therefore the depth of the chamber and remains fixed, Fig. 1.

To initiate ignition sequences, the metallic plate holds an aeronautical spark plug which delivers 450 mJ/pulse and can be localized in front of a given injector as shown in Fig. 2. The height at which the energy is deposited is fixed to $z = 23$ mm above the chamber bottom wall which corresponds to the swirler exits. Swirled injection systems are similar to the one used in [7] and are composed of two admissions (Fig. 3 (a)). In the center, a tube ($d = 4$ mm) acts as fuel injector, surrounded by a radial air swirler ($D = 20$ mm). Methane and air mass flow rates are respectively

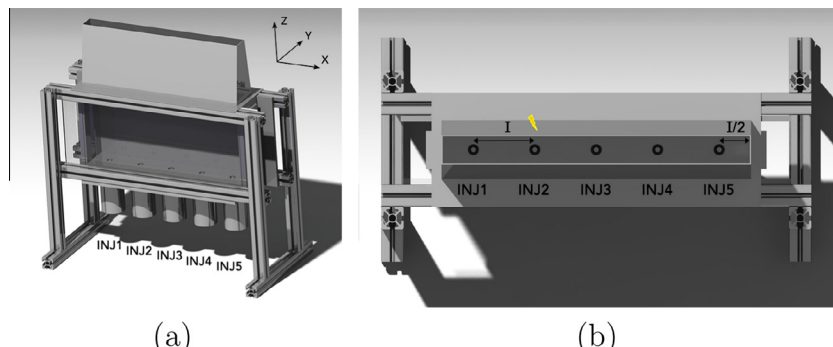


Fig. 1. Sketch of the experimental KIAI multi-burner setup equipped with 5 injectors (left: side view. right: top view).

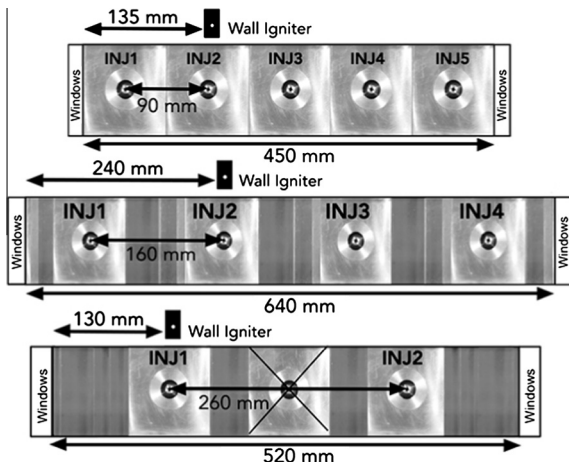


Fig. 2. Scheme of the KIAI multi-burner setup with 5, 4 and 2 injectors, i.e. spacing of $I = 90$ mm, $I = 160$ mm and $I = 260$ mm respectively.

0.192 g/s and 5 g/s for each individual injector, leading to a global equivalence ratio of 0.66. The radial swirller is composed of 18 vanes inclined at 45°. Swirl number is here evaluated at 0.76 [7]. A plenum is used to tranquilize the flow before entering the injection system. Note that a grid is placed in the lower part of the plenum to destroy the large structures of the flow issued from the upstream air feeding lines. Many experimental campaigns have been conducted as detailed in Table 1. All initial or statistically stationary flows operate at ambient conditions.

Three different mechanisms of flame propagation are observed experimentally for the different spacings. It is important to note that as the number of injectors in the combustor is reduced to allow large spacing, the overall thermal power of the test rig is also reduced since the mass flow rates through each injector is constant.

2.1.2. Experimental diagnostics

In order to evaluate the velocity magnitude and turbulent kinetic energy in the combustion chamber, Particle Image Velocimetry (PIV) is used. The PIV system relies on a dual-cavity Nd:YAG laser (Big Sky) and a CCD camera (LaVision Image ProX, 2048 pix²) equipped with a 50 mm Nikkor lens (f/1.2). The laser produces a 120 mJ/pulse at 532 nm at a repetition rate of 10 Hz send in a flow seeded with DEHS (Di-Ethyl-Hexyl-Sebacate) droplets. Post-processing is done using a commercial, multi-pass adaptive window offset cross-correlation algorithm (Dantec Dynamic Studio V3.20). The final PIV window size measures 16 * 16 pix² with an overlap of 50%. Converged statistics are obtained by recording 1000 images for each condition.

Planar Laser-Induced Fluorescence (PLIF) on a tracer is commonly used to measure fuel concentration [14]. This technique is applied to this configuration to quantify the mixing between air and fuel, the flammability limits and the various statistics of equivalence ratio. For these measurements, a tracer (acetone) is added and molecularly mixed with the fuel. A single Nd:YAG laser (Spectra Physics) internally quadrupled to produce a 266 nm laser beam with a typical pulse energy of 130 mJ/pulse is used in this case. The acetone fluorescence signal is recorded with a PI-MAX III:512 Intensified CCD camera with a 512 × 512 pixels array. The images are then digitized with a 16 bit precision. Using a 50 mm Nikkor lens (f/1.2), a magnification ratio of 5.6 pixel/mm is obtained. The intensifier is gated at 500 ns. To optimize and control the acetone concentration into the fuel, liquid acetone is injected through a nozzle and vaporized inside a tank. The acetone flow rate is chosen to get an acetone concentration of 15% in volume in the methane flow. In order to obtain a quantitative measurement of the fuel concentration, the images of the measured fluorescence are corrected by a number of influence according to the methodology detailed by Degardin et al. [15].

For ignition transient characterization, the temporal evolution of the flame growth is obtained from two different high speed flame emission recordings. A qualitative analysis of the heat release zone behavior is achieved, from the time of energy deposition

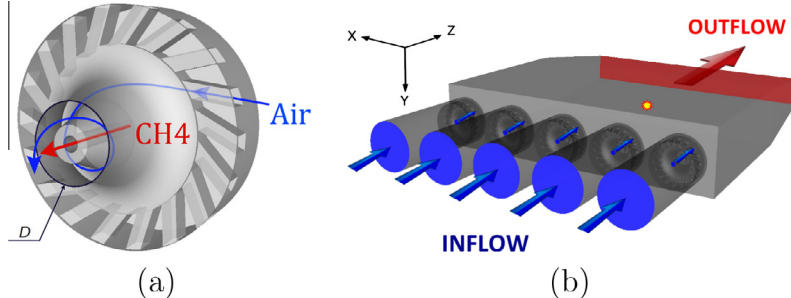


Fig. 3. (a) Details of the injection system for each injector. (b) Computational domain of the SP9 configuration along with the reference cartesian frame (X,Y,Z).

Table 1

Experimental and numerical flow conditions investigated. italicized rows correspond to cases investigated numerically.

Experimental setup				LES setup		
Name	Spacing (mm)	Total Air mass flow rate (g/s)	Injectors	Number of		LES names
				Elements	Nodes	
SP9	90	25	5	37.7 M	6.8 M	SP9
SP13	130	25	5			
SP15	150	20	4			
SP16	160	20	4	43.1 M	7.7 M	SP16(1) and (2)
SP18	180	15	3			
SP20	200	15	3			
SP22	220	15	3			
SP24	240	15	3			
SP26	260	10	2	21.2 M	3.8 M	SP26

by the spark until flame stabilization or misfire. The detection system consists of a Photron SA1 camera (1024×512 pix 2 , 12 bits) and a Photron HighSpeedStar (1024×512 pix 2 , 12 bits) with a repetition rate fixed at 3000 fps, corresponding to an interval time of 333.3 μ s between two successive images. One camera is placed in front of the combustion chamber, and the other one at the top of the combustion chamber, to capture simultaneously flame growth in the (X,Z) plane and in the (X,Y) plane (Fig. 3), respectively. The field of view is varied to always observe the whole configuration. Twenty recordings are carried out for each ignition point. In the following, a detailed analysis of the obtained movies is carried out to present the most relevant ignition scenarios.

2.1.3. Ignition procedure

Experimentally, mass flow meter of air and methane are first switched on and a 15 s delay is necessary to obtain a stationary behavior. For an ignition sequence, after the previous 15 s transient, energy is delivered by the spark. In case of successful ignition defined by fully anchored and swirled stabilized flame in front of each burner, methane is switched off while air flow is maintained to cool down and purge the combustion chamber. After 2 min, a new ignition test is initiated. In case of misfire, a couple of seconds are necessary to ensure no “history” effect.

2.2. Numerical setup

Conjointly to the experimental study, a numerical investigation is conducted using LES. A fully compressible, multi-species LES solver (AVBP) is used to compute the non-reacting stationary flow as well as the ignition sequences.

2.2.1. CFD solver

AVBP is a massively-parallel finite-volume code for the simulation of compressible reacting flows [16], developed by CERFACS and IFP-EN, that solves the Navier-Stokes equations explicitly on unstructured and hybrid grids. It relies on the cell-vertex discretization method [17] and treats boundaries according to the Navier-Stokes Characteristic Boundary Conditions (NSCBCs) formalism [18,19]. The code handles multi-component reacting flows [20] by the use of thermo-chemistry tables and Arrhenius-type chemical schemes. AVBP provides high-order numerical schemes of the continuous Taylor-Galerkin family [21], among which the TTGC scheme, which is third order accurate in time and space.

2.2.2. Simulated configurations

Because of the prohibitive numerical cost of such simulations, the LES study focuses on three configurations at which experiments identified distinct propagation modes. LES cases are listed in Table 1 along with the main figures of the numerical setups. A single ignition sequence is conducted for the SP9 and SP26 cases, while two ignition sequences triggered at distinct times are simulated at a spacing of 160 mm (SP16(1) and SP16(2)) to study the impact of the flow conditions at the time of spark discharge.

2.2.3. Computational mesh and wall treatment

The computational domains retained for all the computations include all injection systems (either 5, 4 or 2) with their individual plenums, swirler veins, fuel nozzles located on the central axis of each injection system, the combustion chamber and the convergent exit (Fig. 3). Note that the numerical domain does not include the grids placed in the plenums. The origin of the coordinates is located at the center of the chamber inlet section.

The geometries are meshed with tetrahedra resulting in fully unstructured grids that are characterized in Table 1. They are refined in the swirler and mixing regions, where the cell size is set to be of the order of 0.25–0.5 mm (Fig. 4). Inlet and outlet conditions impose mass flow rates. Walls are treated with a no slip condition and the WALE subgrid model [22] is used to represent the sub-grid energy dissipation.

2.2.4. The energy deposition ignition model

In the experiment, ignition is achieved by using an electric spark plug located on the lateral wall close to INJ2, therefore at a varying X-coordinate depending on the configuration, the other two directions being fixed to $Z_{spark} = 23$ mm and $Y_{spark} = 45$ mm (Fig. 2). For the transient LES, the Energy Deposition (ED) [23] ignition model is used to describe the electric spark as a source term added to the energy equation with a Gaussian shape in space and time, inducing the formation of the initial kernel. The source term is described by three parameters: the energy transmitted to the gas ϵ_i , the spark duration σ_t and its size σ_s . Experimentally, the used aeronautical spark plug delivers 450 mJ/pulse but the actual energy delivered to the mixture is much smaller than the energy passing through the spark electrodes. Energy loss caused by heat losses, shockwaves and radiation are assumed to reduce to the energy transferred to the fresh mixture to 10–30% of the electric power of the spark [24–26]. In the present cases, the parameters are set to the following values: $\epsilon_i = 135$ mJ (30% of the total energy), $\sigma_t = 300 \mu$ s and $\sigma_s = 15$ mm, in agreement with data retrieved for most aeronautical spark plugs and the material used by experimentalists. As the flame kernel formation is a small size but laminar phenomenon, the impact of the LES combustion models must be minimized. A second computational mesh is used for the first instants of ignition in order to resolve correctly the imposed steep temperature profiles and the resulting reaction zone. This second mesh is refined locally around the energy deposit zone (~ 0.15 mm) so that the thermal thickness of the flame is discretized by 6 grid nodes. Once the flame kernel has reached the border of the refined zone, an interpolation onto the main mesh is performed to re-activate the LES combustion models in the ignition zone and pursue the calculation.

2.2.5. Turbulent combustion and chemistry modeling

The simulations performed in the present work require modeling of the turbulent combustion source term present in the filtered LES governing equations. Chemistry is described with the 2S_CH4_BFER two-step scheme, using Pre-Exponential constant

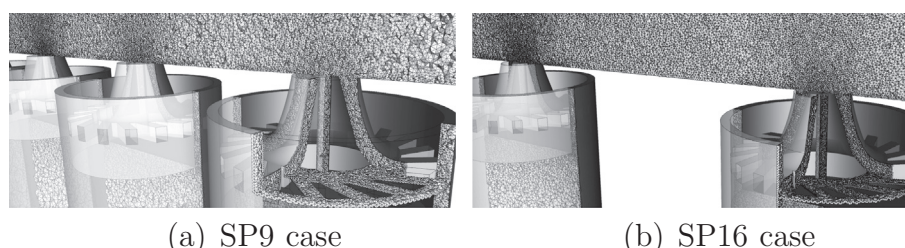


Fig. 4. Slice of the computational domain showing the mesh refinement in the injector vicinity for SP9 (a) and SP16 (b) configurations.

Adjustment (PEA) [27] to match the flame speed in the whole range of flammable equivalence ratio. To comply with the PEA correction, simplified transport properties are assumed for species and heat diffusion coefficients. As required by PEA, the same Lewis number is used for all species so that differential diffusion effects are suppressed. With these hypotheses and the conditions of the considered configuration, i.e. $\Phi = 0.66$, fresh gas temperature $T = 298\text{ K}$ and pressure $P = 101325\text{ Pa}$, the two-step scheme for CH_4/Air combustion gives a laminar flame speed $S_l = 17\text{ cm/s}$ and a flame thickness of $\delta_l = 0.815\text{ mm}$. The interaction between combustion and unresolved small-scale turbulence is modeled by the Dynamic Thickened Flame (TFLES) model [28,29]. This approach artificially thickens the flame front by a factor F to resolve it on the LES grid, while the unknown sub-grid scale flame-turbulence interaction is modeled with an efficiency function \mathcal{E} [28].

3. Cold flow predictions and validation

Prior to study the transient phenomenon occurring during ignition, experimental and numerical isothermal results are used conjointly to identify the major structures of the flow and point out the changes induced by an increase of the spacing between injectors. The first two statistical moments are obtained by time-averaging. Statistical quantities are collected for 35 ms for the SP9 and SP16 cases and 18 ms for the SP26 configuration.

3.1. Flow structures

All individual injectors produce a similar flow structure, with 3 typical zones of swirling flow as clearly identified in Fig. 5. Swirled Jets (denoted hereafter SWJ) are characterized by their high swirling motion. They appear to be symmetric when time-averaged and extend far downstream the chamber. An Inner Recirculation Zone (IRZ) is also observed downstream each injector along their central axis. These are typical of swirled flows with swirl numbers above the critical value of 0.6 [30]. IRZ competes with the central injection of methane producing a stagnation point, already observed in [7,31]. For all injectors, the stagnation point is located approximately 10 mm downstream the injection fuel nozzle and its immediate vicinity presents a highly turbulent behavior. This is explained by the fact that this point location is not perfectly stable but moves around a mean position due to large flow instabilities [32]. Finally, Lateral Recirculation Zones (LRZs) are located between the SWJ of neighboring injectors and are bounded at the top by the meeting of two SWJ. LRZ feature low levels of velocity and turbulent kinetic energy. Large size counter-rotating vortices are observed within

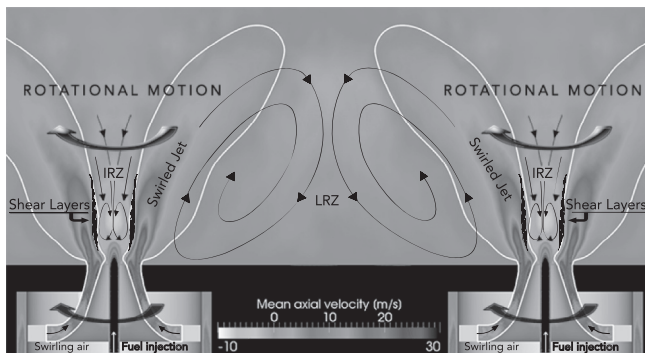


Fig. 5. Characteristic zones of a swirled flow. Grayscale corresponds to the LES time-averaged Z-component velocity in a Y-normal cut. The white line highlights the limits of the SWJ and schematic arrows illustrate fluid motion in both IRZ and LRZ.

LRZ, inducing slow recirculation. The width and height of LRZ are found to be directly linked to the spacing between injectors as will be evidenced later on. Note also that for all cases, a global circumferential flow appears (Fig. 6). Its origin comes from the local entrainment induced by all the individual swirling flows. This global feature is clearly impacted by the injector spacing and is lower for larger inter-injector distances. The overall induced circulation is indeed directly proportional to the number of swirlers and the chamber section.

To provide a better understanding of the different recirculation zone shapes observed in the configurations of Table 1, projected time-averaged streamlines are shown on a y-normal mid-plane in Fig. 7. For the SP9 case, because of the immediate vicinity of injectors, the swirled branches of neighboring injectors interact very rapidly. This leads to larger IRZ ensuring strong gas recirculation towards the injection system and a larger opening of the SWJ. The LRZ has a relatively small height h (of the order of $h/D \sim 2.5$). Note that for this case, no clear rotating motion is evidenced in the LRZ. For the SP16 case, the behavior of the flow slightly differs. The SWJ extend further downstream with a narrower opening angle, generating a larger LRZ composed of two weak counter-rotating vortices. The height of the LRZ is for this SP16 case of the order of $h/D \sim 4$. Note that these two vortical structures influence the jet opening angle in its top part. Similarly, the SP26 case presents a more constricted IRZ and a larger LRZ (with a height h/D of ~ 6.5) than the SP9 and SP16 cases. This large spacing configuration is also characterized by a total absence of direct interaction between SWJ. Such changes in time-averaged flow structures are expected to strongly impact the flame propagation mechanism, as will be detailed later.

3.2. Comparison between numerical simulations and experiments

3.2.1. Time-averaged velocity profiles

The accuracy of the previously described LES results is evaluated by comparing time-averaged velocity profiles to experimental data at 3 axial positions corresponding to $z/D = 0.25; 1; 1.5$ in the local cylindrical reference frame (r, θ, z) associated to one specific injector: i.e. with origin located at the bottom end of the whole chamber on the center-line of the injector of interest.

Figure 8 displays the comparison of the axial and radial components for the SP9 case. For this configuration, the simulation captures well the 3 typical zones of the swirling flow. The location of the stagnation point is also well recovered and the SWJ opening as well as recirculation zone sizes are reproduced. The magnitude of the time-averaged axial and radial velocity components is

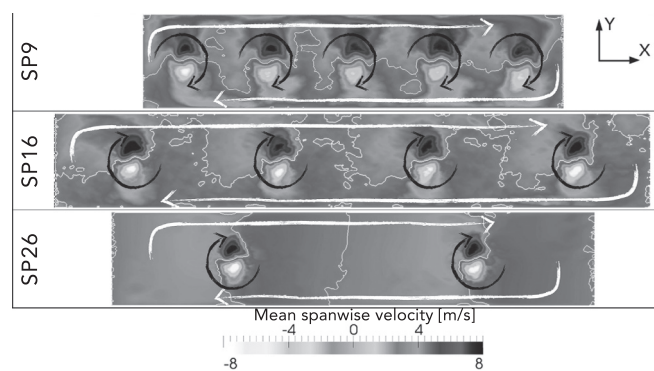


Fig. 6. LES results: global circumferential flow of the SP9, SP16 and SP26 configurations. Grayscale corresponds to the time-averaged X-component velocity in a Z-normal cut.

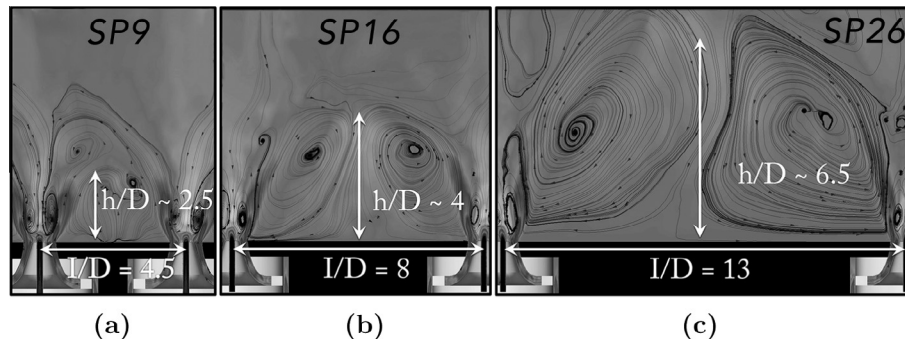


Fig. 7. LES results: time-averaged 2D flow streamlines in the Y-normal cut highlighting the recirculation zones respectively for SP9 (a), SP16 (b), and SP26 (c) cases. An estimation of the width and height of LRZ is also provided for each case.

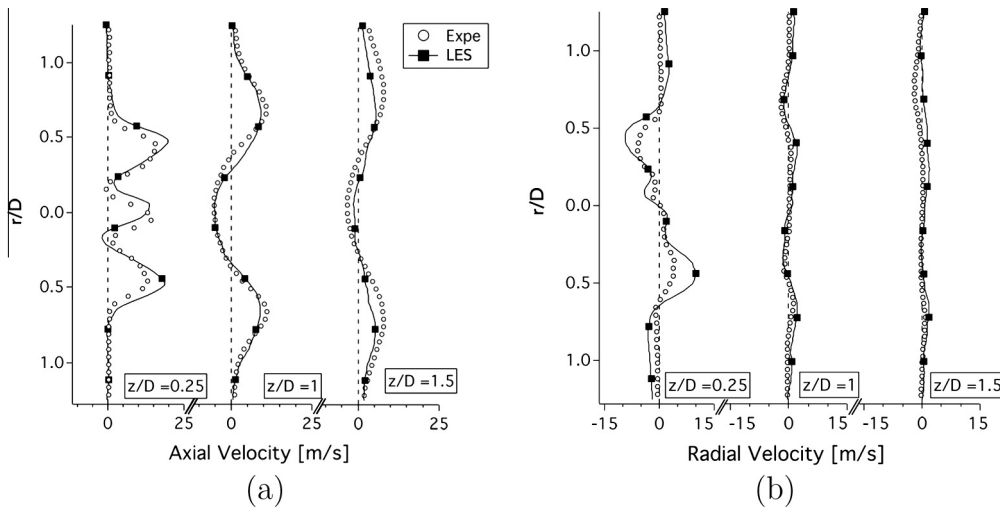


Fig. 8. Experiments versus LES: time-averaged axial (a) and radial (b) velocities for the SP9 case.

overall satisfying compared to measurements. Similar results are obtained for the SP16 and SP26 cases when compared to experimental data (not shown here).

Figure 9 details the shape of the SWJ for the three configurations. The jet opening is clearly larger in the SP9 case and the angle decreases with increasing injector spacing. No substantial differences are observed on the time-averaged radial velocity profiles between the three cases.

3.2.2. Mixing

Mixing is assessed by comparing the equivalence ratio profiles of LES and experiments shown in Fig. 10. LES results are in good agreement with measurements for the 3 cases, identifying homogeneous mixtures in the LRZ thanks to the rapid mixing between air and methane after injection. It is also noted that mixing is slightly more efficient for larger spacing, probably due to a narrower SWJ opening. The experimental measurements for the

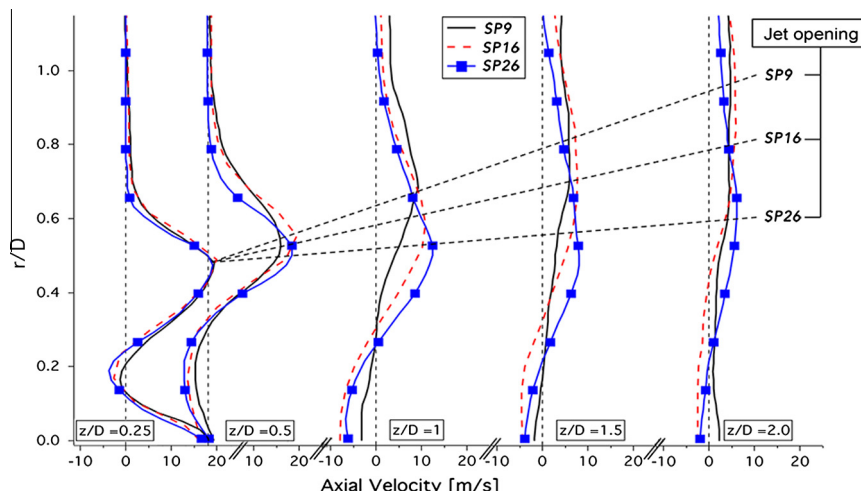


Fig. 9. LES: time-averaged axial velocity component illustrating the jet opening angle obtained in the three configurations.

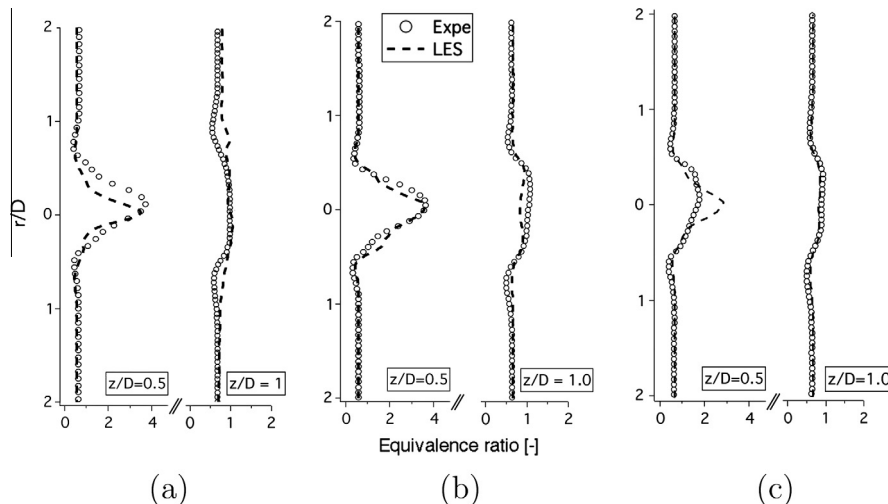


Fig. 10. Experiments versus LES: time-averaged equivalence ratio for the SP9 (a), SP16 (b) and SP26 (c) configurations at two axial locations (time-averaging is performed over 35 ms, 35 ms and 18 ms respectively).

mixture fraction fluctuations [33] show that the equivalence ratio fluctuations further than $z/D = 0.5$ and $r/D = 0.75$ are negligible, and so we can treat the flame evolution from the spark location with premixed flame concepts mainly.

4. Ignition sequences

Flow conditions at the ignition time play a major role in the ignition process [34,8] and are presented first. Flame dynamics are then described and analyzed using instantaneous snapshots extracted at several key instants of the ignition sequences, from both experimental and numerical data, with a complementary analysis based on the flame kernel position for the SP9 et SP26 configurations. The overall ignition delays are finally presented and compared to measurements, demonstrating the relevance and accuracy of LES for such phenomena.

4.1. Flow conditions at ignition time

Both experimentally and numerically, the spark deposits energy close to the wall at an axial position of $z/D = 1.15$ which corresponds to a location where the mixture is quite homogeneous and turbulence is low as seen in Section 3.2. Figure 11 shows the stationary flow state at the location of the spark plug for the 3 cases investigated numerically. It is interesting to note that energy

deposition takes place in a zone of positive axial velocity for one case only, corresponding to very large injector spacing (SP26).

To evaluate the role of the cold flow state, for the intermediate spacing case (SP16 configuration), two ignition sequences (SP16(1) and SP16(2)) are performed, starting at two different instants (t_1 and t_2) of the stationary cold flow. The first instant is chosen arbitrarily while the second is chosen so that the flow at the spark is significantly different from the flow at t_1 . In particular higher spanwise velocities and negative cross-stream velocities in the ignition zone are observed at t_2 (Fig. 12).

The time evolution of the cold flow velocity components at the spark location is detailed in Fig. 13. The profiles are shifted in time to place the instant of ignition at $t = 0$ ms. Ignition in the SP9 configuration is performed in a zone presenting high positive spanwise velocity while the SP16 and SP26 cases present a lower component (Fig. 13(a)) partly induced by the lower circumferential mean flow. Axial velocities are slightly higher in the SP16 case than in the SP9 case, but still have negative values while in the SP26 case the change in confinement places the energy deposition in a zone of positive axial velocity as seen in Fig. 11.

4.2. Flame propagation modes

Experiments and simulations clearly identify three different mechanisms of flame propagation, specific of three spacing ranges.

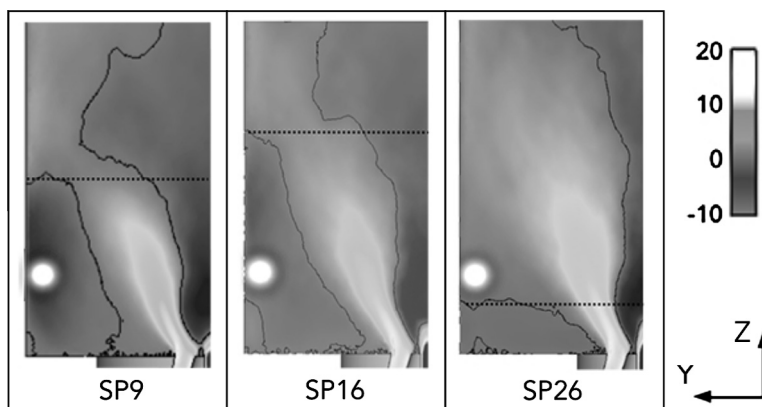


Fig. 11. LES results: schematic view of the spark plug location ($z/D = 1.15$). Grayscale: time-averaged axial velocity, dashed lines: height of the LRZ, solid lines: iso-contour of zero axial velocity.

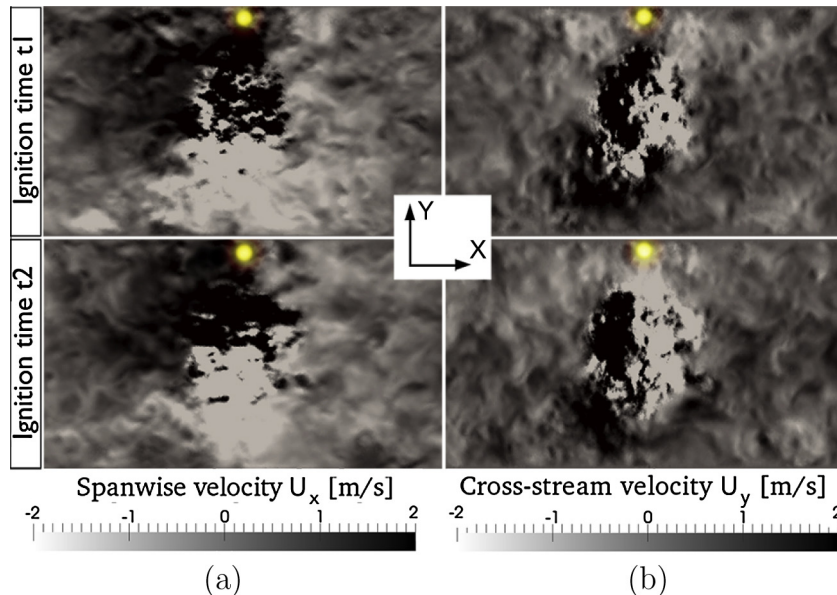


Fig. 12. LES results: 2D Z-normal cut at the ignition axial position close to INJ2. Instantaneous spanwise (a) and cross-stream (b) velocity components at the two different ignition times (cases SP16(1) and SP16(2)). The spark plug is also represented.

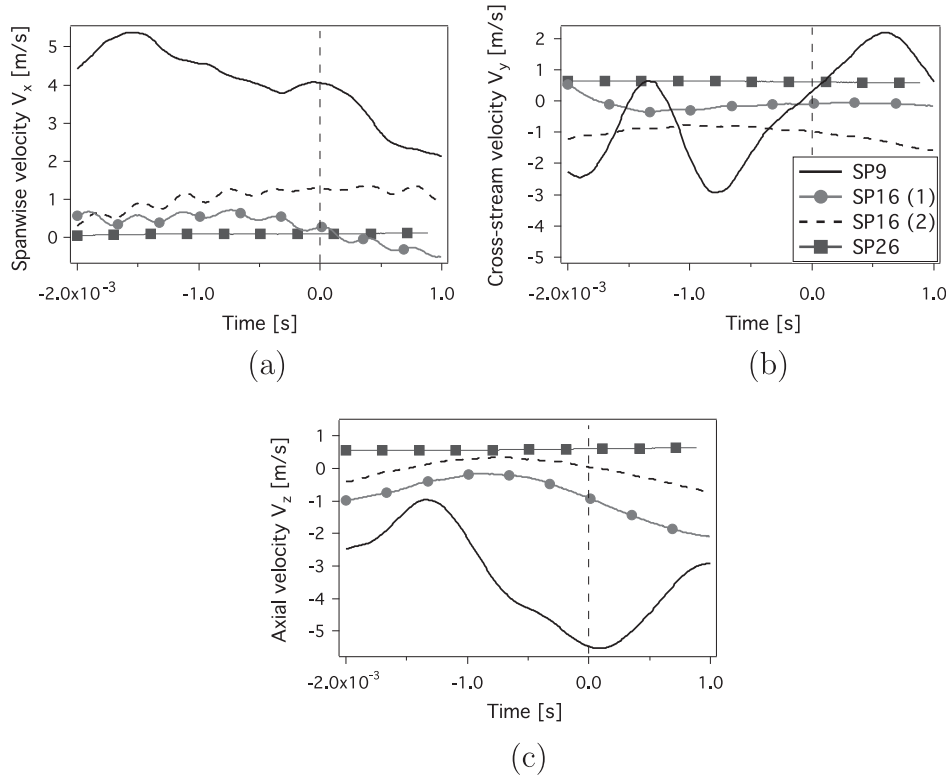


Fig. 13. LES results: temporal evolution of the instantaneous velocity spanwise (a), cross-stream (b) and axial (c) components at the spark location for each case.

All three mechanisms are described and analyzed below combining experimental and numerical results. In this analysis, ignition of an injector is considered successful once the flame is attached to the injector nozzle.

4.2.1. Spanwise flame propagation

The first ignition mechanism is identified for spacings ranging between 90 mm and 150 mm and is illustrated on the SP9 configuration. Figure 14 presents snapshots of the signal recording of the

experiments that account for the CH and C2 light emissions. LES visualizations of volume rendering of heat release for the same case are shown in Fig. 15. In both figures, the times of visualization are the same and correspond approximately to the successive ignition of each injector. Despite the stochastic nature of ignition, experiments and LES agree well on both the successive injector ignition order and the time delay between them.

Early after sparking, the flame interacts directly with the nearby injector swirling flow (INJ2). Then it is rapidly swept by the flow

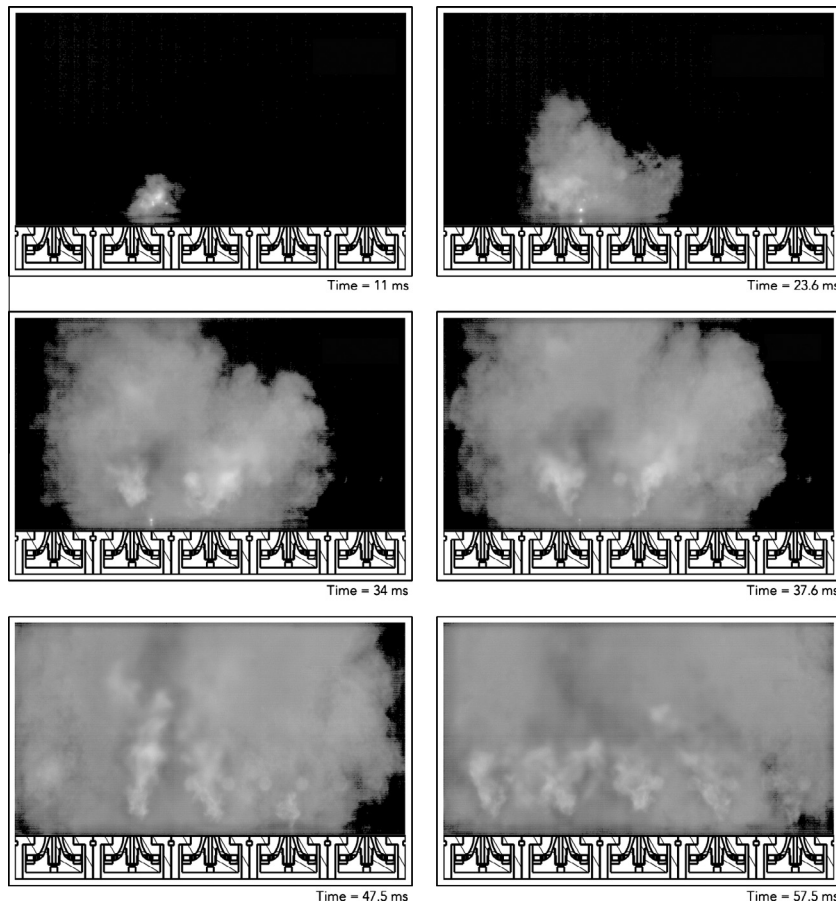


Fig. 14. Experiments: fast visualization of the flame showing a spanwise propagation for SP9 case.

induced by INJ2 and INJ3 leading to the birth of two distinct branches as shown in Fig. 15 ($t = 11$ ms). As time proceeds, the flame follows essentially a lateral/spanwise motion in the bottom part of the chamber. This spanwise flame propagation process keeps on spreading at $t = 23.5$ ms (Figs. 14 and 15) with still a pronounced winding around the injector while the flame reaches INJ2. The following LES successive ignitions of INJ3 and INJ4 occur at $t = 34$ ms and $t = 37.5$ ms respectively, slightly before the corresponding events in the experiments. The strong expansion of burnt gases leads to a large amount of burnt gases at the exhaust at this time. The last two injectors are reached by the flame lastly approximatively at $t = 47.5$ ms and 57.5 ms (60 ms for experiment) to finally obtain fully stabilized flames on all injectors.

Figure 16 shows a quantitative evaluation of the flame propagation based on flame contour detection and flame front position calculation from instantaneous snapshots, in the axial and spanwise directions. The radius is evaluated as the distance between the initial flame kernel position and the flame spanwise or axial location. A quasi isotropic evolution of the flame front is observed experimentally while numerically, the flame development is non-isotropic with a larger spanwise radius. Note that the results are averaged over 10 experimental ignition sequences while a single LES realization is available which might explain the offset between experimental and numerical findings.

4.2.2. Axial flame propagation

The second ignition mechanism is found for the largest spacings, between 200 mm and 260 mm. It is mainly dominated by an axial flame propagation. Figures 17 and 18 present ignition sequences obtained for the largest spacing configuration SP26 in experiments and

LES respectively. Both the ignition time of the first injector and the subsequent delay to ignite the second injector obtained in LES are in good agreement with the experimental results.

After the spark, the flame kernel survives but no increase of flame surface is observed for a few milliseconds (Fig. 17, $t = 14$ ms). During this time, the flame remains sensitive to extinction. Then, the flame develops and is mainly convected in the axial direction (Figs. 17 and 18, $t = 14$ ms). As time proceeds, the flame expands in a region confined between the SWJ of INJ1 and the wall. It starts filling the top of the combustion chamber until a fragment is captured by the IRZ to propagate upstream and finally ignite INJ1 at $t = 46.2$ ms in LES and $t = 54.3$ ms in experiments (Fig. 22). The flame extends far downstream and is eventually captured by the IRZ of INJ2 to ignite it at $t = 117$ ms and $t = 137.3$ ms in experiments (Fig. 22). Ignition of INJ2 requires the flame to circumvent the SWJ and penetrate the IRZ but due to the high turbulent behavior of the SWJ, the ignition time of INJ2 is subject to high fluctuations. Note that in real combustors, such flame propagation mechanism is not likely to occur when secondary air dilution is present.

The quantitative evaluation of the flame propagation reveals in this case a non-isotropic evolution (Fig. 19). For both LES and experiments, the axial flame radius is higher than the spanwise one and differences increase with time. These trends completely differ from SP9 configuration (Fig. 16), confirming the different propagation mode.

4.2.3. Hybrid flame propagation

The third ignition mechanism is observed for intermediate spacings between 160 and 180 mm and is illustrated in SP16 in Figs. 20 and 21 for experiments and LES respectively.

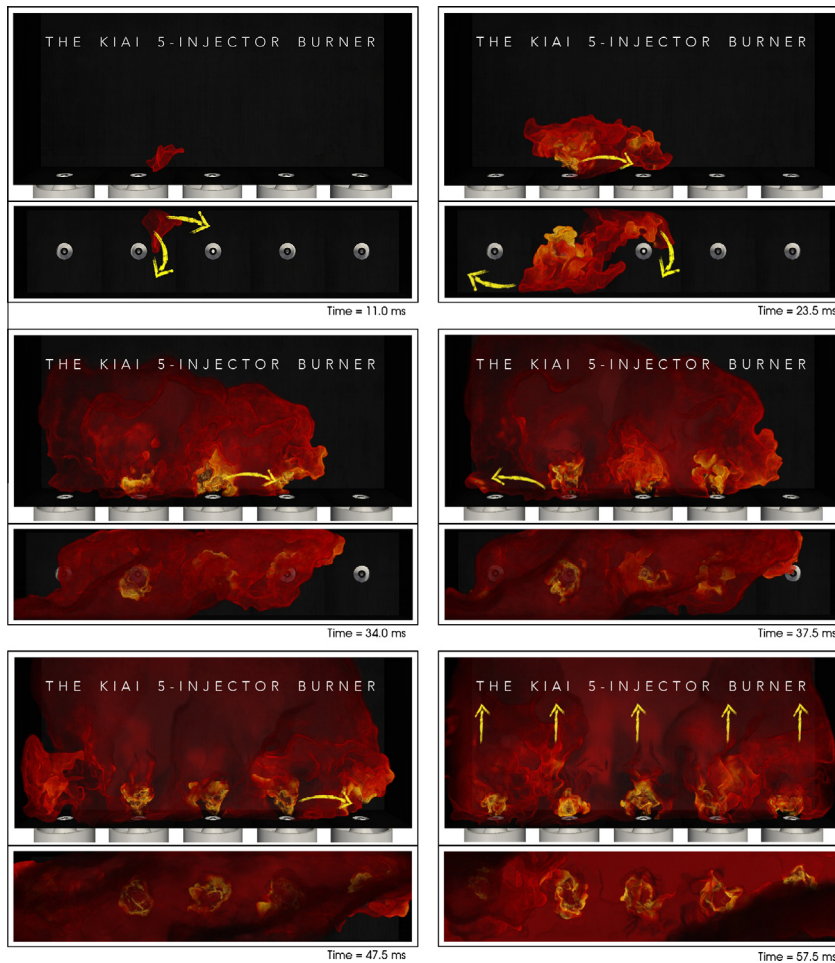


Fig. 15. LES results: instantaneous snapshots of the SP9 ignition sequence visualized by the volume rendering of heat release (front and top views).

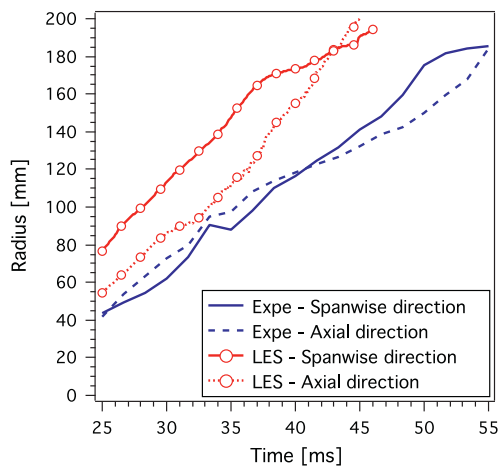


Fig. 16. Experiments versus LES: estimations of local flame propagation for SP9 case.

After the kernel creation, low flame development or convection is observed in both axial and spanwise directions while the flame is rapidly swept by the SWJ of INJ2 (Figs. 20 and 21, $t = 14$ ms). Once INJ2 is ignited, a flame front propagates on each side, where a hybrid propagation mode is observed with competing spanwise and axial motions. Figures 20 and 21 at $t = 48$ ms or 57 ms show pathways of the flame front (highlighted with arrows). The flame front

is convected by the SWJ and fills the IRZ in the axial direction to a certain extent, while it also propagates in the spanwise direction in the low velocity LRZ under the action of the volumetric burnt gas expansion. Early after sparking the SP16(1) exhibits a more axial flame development as compared to SP16(2) due to the different initial flow conditions (Fig. 21) delaying the spanwise flame propagation. This initial time delay is further increased as time proceeds since in the SP16(2) the flame front follows a more spanwise pathway in the lower part of the combustion chamber while in the SP16(1) a flat flame front is observed (Fig. 21 at $t = 57$ ms).

4.3. Ignition delays

The successive ignition times of each individual burner as well as the overall ignition delays are identified in the LES through a specific criterion that can be compared to experiments.

4.3.1. Ignition delays of individual burners

As the flame reaches the injector location, it eventually penetrates and stabilizes in the IRZ. When the flame enters the lower part of the IRZ, the richer mixture induces higher light emission in the experiments. Similar behavior is observed in the LES visualization of heat release and is used to evaluate ignition times in both experiments and simulations. The methodology consists in detecting visually the sudden heat release increase on the recordings. Note that in experiments, multiple tests also provide an evaluation of variability. This methodology is obviously associated to some

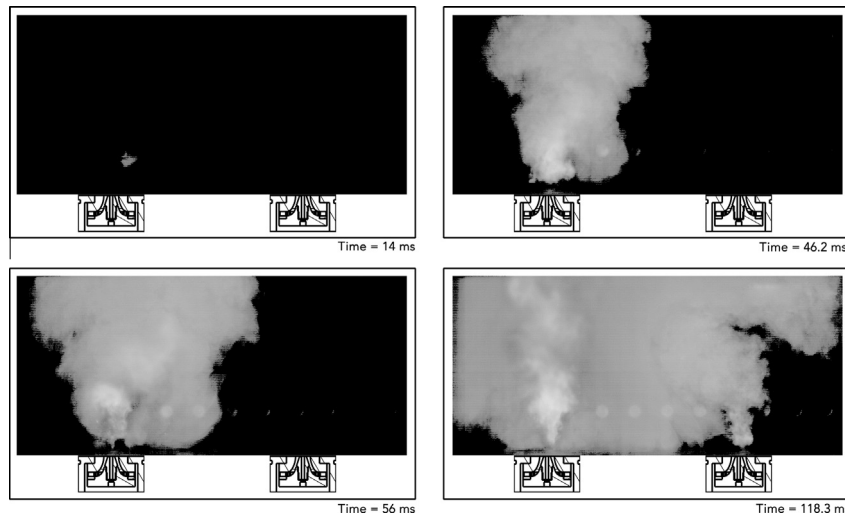


Fig. 17. Experiments: fast visualization of the flame showing an axial propagation for SP26 case.

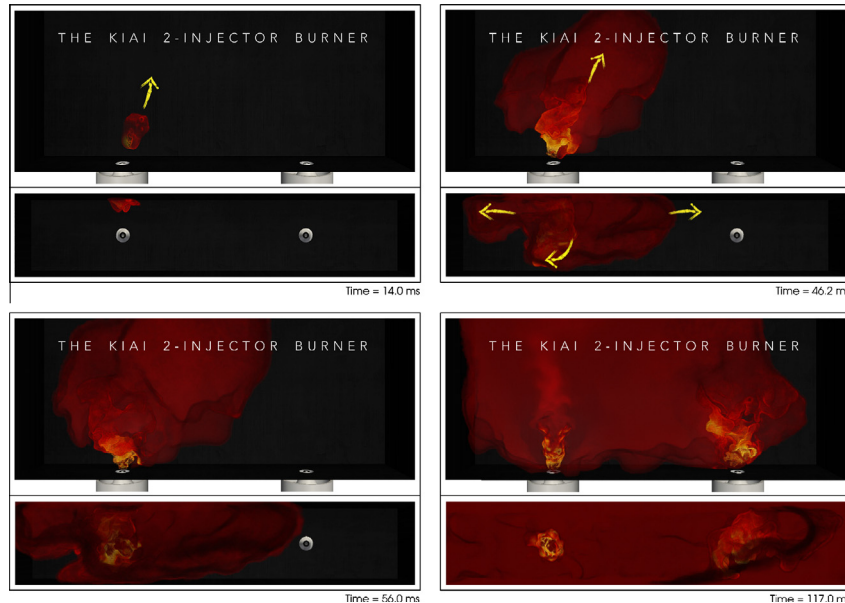


Fig. 18. LES results: instantaneous snapshots of the SP26 case ignition sequence visualized by the volume rendering of heat release (front and top views).

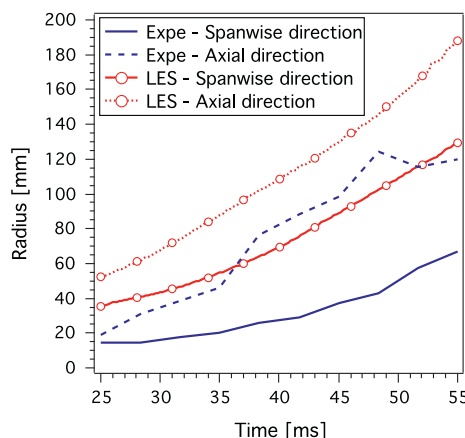


Fig. 19. Experiments versus LES: estimations of local flame propagation for SP26 case.

uncertainty and it has been evaluated with a more quantitative approach based on the mean heat release in the IRZ extracted from LES data in the SP9 case.

Individual injector ignition times are listed in Fig. 22 for experiments and LES. The first observation from Fig. 22 is the good agreement between LES and experiments concerning the delays between successive injector ignition times. These results show that LES accurately reproduces the propagative phase of the ignition sequence. The order of injector firing is directly linked to the flame propagation dynamics in the combustion chamber described in Section 5. A 10 ms offset is estimated between the simulated ignition time of INJ2 and the mean experimental one in the SP9 case and reported in all cases. The origin of this offset may come from the uncertainty of the kernel created by the ED model, the transition from a laminar flame kernel to a turbulent expanding flame that is not perfectly handled by the combustion model and the uncertainty of the above methodology for the ignition time estimation.

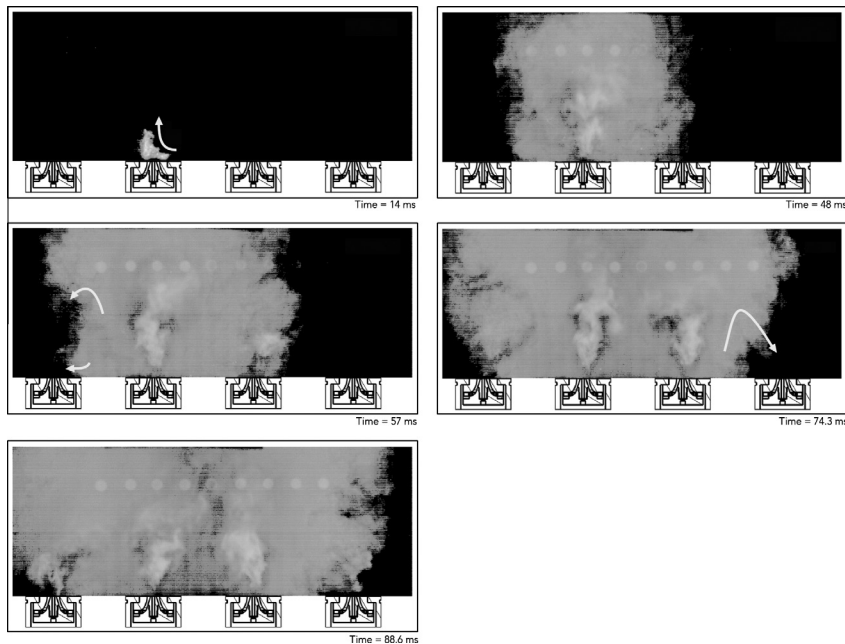


Fig. 20. Experiments: fast flame visualization showing a hybrid propagating mode for SP16 case.

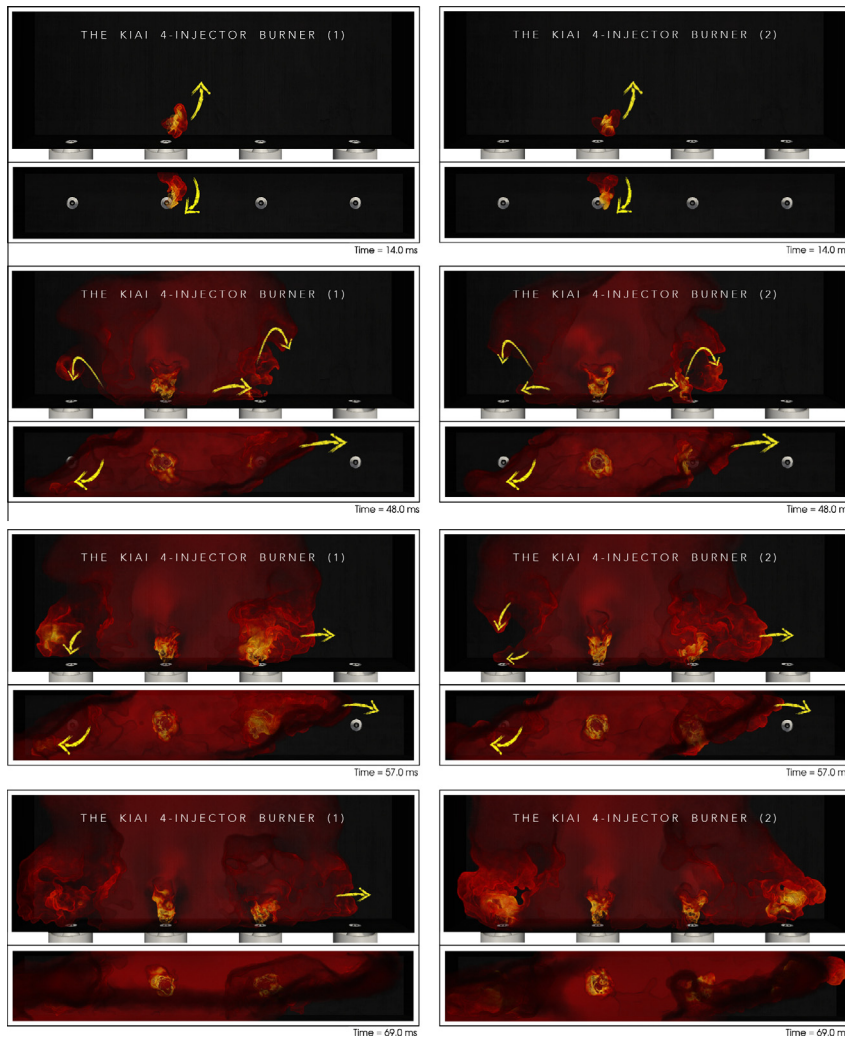


Fig. 21. LES results: instantaneous snapshots of SP16(1) (left) and SP16(2) (right) ignition sequences visualized by the volume rendering of heat release (front and top views).

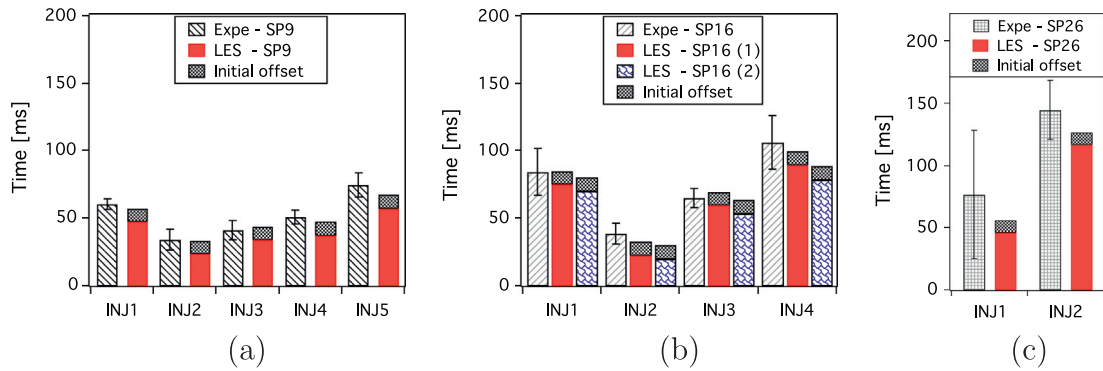


Fig. 22. Experiments versus LES: injectors successive ignition times (ms).

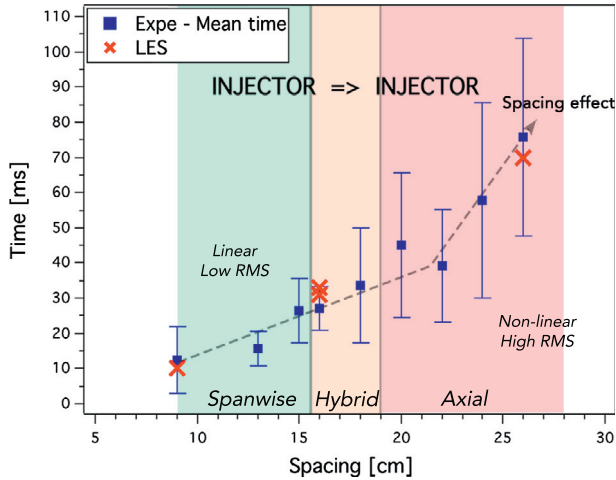


Fig. 23. Experiments versus LES: spacing effect on the first injector/injector propagation time.

4.4. Effect of spacing

Another interesting feature for the design of the burner is the injector to injector flame propagation time. It is evaluated here between the first and second injector ignition and is shown in Fig. 23 where experimental data is averaged over 20 ignition tests and numerical results correspond to a single realization. Error bars on the experimental points show the variability of the experimental results. The agreement between LES and experiments is excellent, demonstrating that LES captures the main controlling processes. Two main trends are identified. The injector/injector time evolves linearly with the spacing in the low spacing range where ignition is governed by the spanwise propagation. Error bars show a low variability in the experiments, qualifying spanwise ignition as a safe mode. For a spacing of 160 mm, the injector/injector time increases more markedly as well as the variability of the experimental results. For large spacings, the propagation from one injector to its neighbor becomes more random and conditioned by the capture of a flame portion by the IRZ of the neighboring injector.

4.4.1. Overall ignition delay

It is difficult to directly measure the heat release integral in the experiment but CH and C₂ light emissions, captured using a high frame rate camera equipped with bandpass filter, are good indicators.

The spatial integration of pixel intensities in both experimental (C₂ and CH emissions) and LES (heat release) snapshots enable to

obtain a comparable line of sight integrated representation of the flame evolution. This is represented in Fig. 24 as a function of time where both quantities are normalized by their respective maximum values. Results show a fairly good agreement, demonstrating again the capacity of LES to capture the main features and mechanisms of the ignition process. It also highlights the much slower growth rate of the SP26 case compared to the SP9 and SP16 cases, and the experimental variability.

5. Mechanisms driving the flame propagation

A simple calculation based on the characteristic length of the combustion chamber and the overall ignition delay evaluates the mean spanwise flame velocity over the complete SP9 sequence at about 5 m/s which is much higher than a typical turbulent flame speed: this means that the flow plays a major role in this process. To evaluate this effect, the displacement flame speed is introduced by splitting the total flame speed into a flow contribution and a self-propagating flame contribution. The impact of the flow structures on the flame propagation is first investigated, followed by a quantitative study of the thermal expansion effect on the flow. Finally, the modulation of the flame structure by the flow is studied as it also contributes to the total flame speed. This study focuses on the extreme SP9 and SP26 cases where the spanwise and axial propagation modes are clearly identified.

5.1. Total flame speed, convective speed and flame displacement speed

Past studies have shown that the competition between convection speed and flame displacement speed plays a crucial role in the

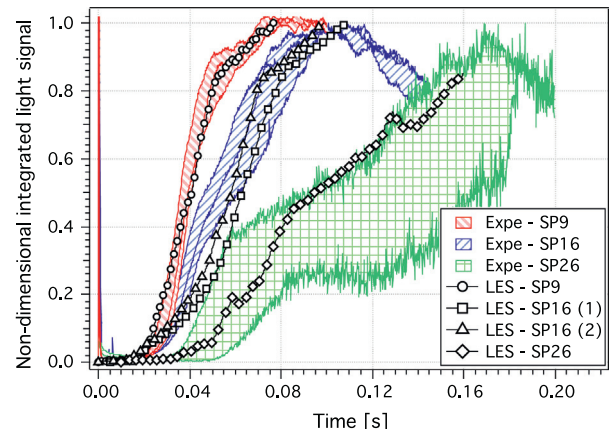


Fig. 24. Experiments versus LES: temporal evolution of the integrated light signal.

success of ignition. In cases of low gas velocity, the flame is able to propagate upstream [4,5] while in configurations with high gas velocity, the flame tends to be convected downstream [5,35,36].

To evaluate the flame displacement speed, the flame front is tracked by an iso-surface of a progress variable here based on the temperature, $c = (T - T_f)/(T_b - T_f)$ where the subscripts f and b correspond to values in fresh reactants ($c = 0$) and fully burnt products ($c = 1$) respectively. The displacement speed of a flame front relative to the flow is defined as the difference between the convective speed $U = \|\vec{u}\|$ and the flame front speed $U_T = \|\vec{u}_T\|$: $S_d = (\vec{u}_T - \vec{u}) \cdot \vec{n}$, where $\vec{n} = -\nabla c / |\nabla c|$ is the normal to the flame front pointing towards the reactants. Using the definition of the progress variable based on the temperature and the transport equation of energy, one finds an expression for S_d [37]:

$$S_d = \frac{1}{\rho C_p |\nabla T|} \left[\frac{\mathcal{E}}{\mathcal{F}} \dot{\omega}'_T + \nabla(\mathcal{E} \mathcal{F} \lambda \nabla T) - \nabla T \left(\rho \sum_{k=1}^{N_{\text{spec}}} C_{p,k} Y_k V_k \right) \right] \quad (1)$$

where $\dot{\omega}'_T$ and V_k are respectively the LES combustion energy source term which includes the effect of the thickening \mathcal{F} , the efficiency function \mathcal{E} and the diffusion velocity for each species k of the mixture. From Eq. (1), it is important to note that S_d is governed by the local balance between molecular diffusion and the reaction. The c iso-surface is classically [37] chosen in the fresh gas side at $c = 0.2$. Choosing a value defined in the fresh gas side minimizes the hot gas acceleration bias due to the volume expansion.

Contributions of S_d and U to the flame front speed are given for the SP9 and SP26 cases in Fig. 25, showing the Probability Density Function (PDF) of the flame displacement speed and the flow speed calculated along the flame front ($0.18 < c < 0.22$) at two different times, taken before and after the flame reaches the SWJ (illustrated in Fig. 15 at $t = 11$ ms and $t = 23.5$ ms for the SP9 case). First, it is remarkable that the flame displacement speed has a much smaller direct contribution to the total flame speed as compared to the flow speed, whatever the number of injectors or the instant considered. Regarding the flow velocity, the PDF at early stages shows lower values in the SP26 than in the SP9 configuration, as expected due to a weaker circumferential motion in the LRZ. After the flame reaches the SWJ, the flow velocity at the flame location is spread over a wide range [0.0–20.0 m/s] in the SP9 case while the main part of the flame surface remains in the range [0.0–5.0 m/s] for the SP26 case since the flame has mainly propagated downstream in low velocity regions. Thus the flame is more convected by the underlying gaseous flow rather than self-propagating.

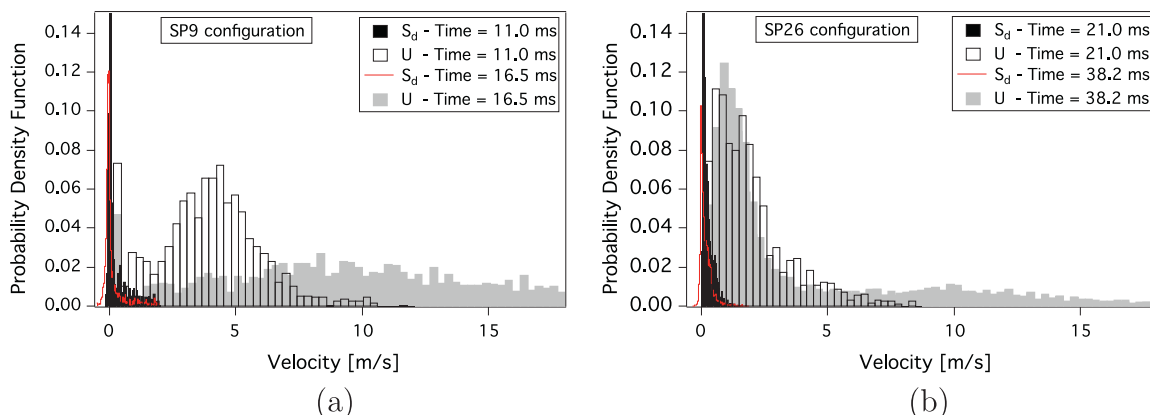


Fig. 25. LES results: PDF of the flame front displacement S_d and the flow velocity magnitude U at two different times before and after the flame reaches the SWJ for the SP9 (a) and SP26 (b) configurations.

5.2. Effect of the flow structures on the flame propagation

The convective flow speed U being the major contribution to the total flame speed, the flow structures are now studied to determine their role in the appearance of either propagation mode.

5.2.1. Flame kernel trajectory

Figure 26 illustrates the different behaviors of the flame kernel motion by describing the Flame Centre of Gravity (FCG) position during the first instants after ignition defined by:

$$x_{i,\text{FCG}} = \sum_{n=1}^N \frac{\rho_n V_n x_{i,n}}{\rho_n V_n} \quad (2)$$

where $x_{i,\text{FCG}}$ is the i th coordinate, ρ_n and V_n the density and volume at the n th node and N the number of nodes having a temperature higher than 600 K. Note that because the energy deposit X_0 -coordinate varies with the three configurations, the relative x -coordinate $X-X_0$ is used in Fig. 26. At the spark location, the flow is dominated by the circumferential motion. The latter is strongest in the SP9 case, promoting a fast convection of the flame kernel in the spanwise direction (Fig. 26(a)), favorable to the spanwise propagation mode. The narrower SWJ in the SP26 case prevents the flame from being quickly swept by the closest injector, and the consequence is a small cross-stream displacement of the FCG as compared to the other cases (Fig. 26(b)). For this case, changes in LRZ shapes (Fig. 9) induce a convection mainly in the axial direction, premise of the axial propagation mode (Fig. 26(c)).

5.2.2. Effects of the swirl motion

As the flame further expands, it eventually meets the strongly rotating flow in the vicinity of the SWJ. To illustrate the interaction of the flame front with the swirl motion, Fig. 27 shows a top view of the combustion chamber with the flame front position in the SP9 case from both experimental and numerical sequence visualizations. Experimental results are obtained by the binarization of images at an adequate light intensity threshold to detect the flame contour. Following the flame kernel convection in the positive spanwise direction, two flame propagation directions can be identified ($t = 14.1$ ms). A first flame branch moves essentially along the metallic plate towards INJ3, following the mean flow circumferential motion. A second branch develops in the cross-stream direction and is rapidly captured by the SWJ of INJ2. While the first branch keeps its spanwise direction, the second one progressively rolls-up around INJ2 ($t = 17.5$ ms and $t = 18.7$ ms) and finally penetrates the IRZ before stabilizing ($t = 21.2$ ms). This flame pathway is also observed for the SP16 cases to a lesser extent and is partially

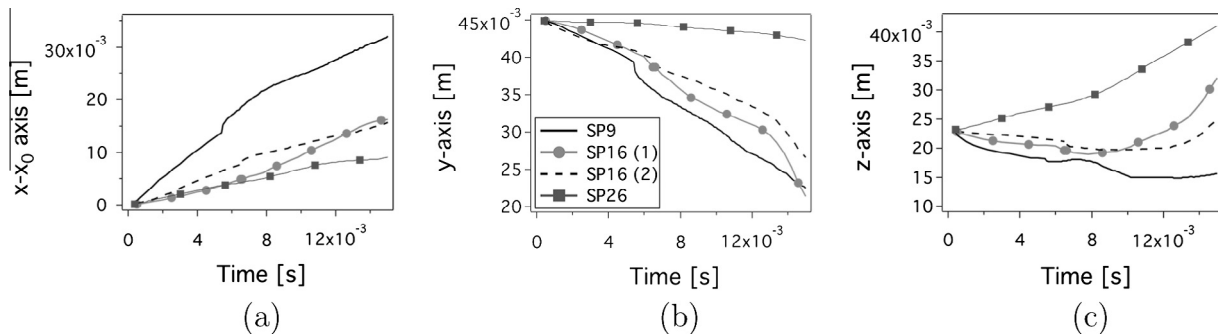


Fig. 26. LES results: Temporal evolution of the position of the FCG during the first instants for the three configurations. (a) spanwise, (b) cross-stream, (c) axial positions.

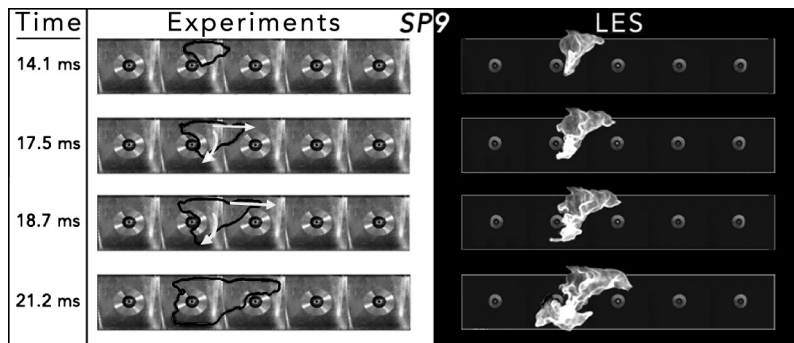


Fig. 27. Experiments versus LES: early stages of flame propagation for SP9 case.

responsible for a strong spanwise motion of the flame of SP9 and SP16 cases. The same roll-up mechanism around is observed INJ3 as for INJ2 but at later time. Such flame motion is further delayed in the SP26 ignition sequence.

This swirl motion is favorable to the spanwise propagation mode and directly impacts the ignition order of injectors since the flame must first roll-up around INJ2 before reaching INJ1 while it quickly convects the flame toward INJ3. In a fully annular configuration, this longer pathway results in a time advance of the flame front located in the favorable direction as observed by Bourguoin et al. [13].

5.3. Thrust effect

Through heat release, the flame introduces strong velocity divergence and modifies the flow. As the flame surface increases, the global consumption rate progressively increases. It eventually reaches a critical value above which the thermal expansion of the large amount of burnt gases becomes a significant mechanism of flame motion by accelerating the fresh gases in front of the flame. This is illustrated in Fig. 28 for the SP9 and SP26 cases at instants when the flame front is spreading between two injectors.

Figure 28(a) clearly shows in the SP9 case the strong interaction between the five high velocity streams due to the five swirlers and the flame, in particular the thrust effect, driven by burnt gas expansion. At the early instants of ignition, the flame location induces an increase of the spanwise velocity, facilitating the flame propagation around the second swirler (Fig. 28(a), $t = 26$ ms). The SWJ of each injector acts as an obstacle that reduces the cross section resulting in very high spanwise velocity between the SWJ and the lateral wall. The flame is then swiftly convected in these regions and this mechanism greatly contributes to the spanwise propagation mode. When the flame front travels in the LRZ, the flow aerodynamic in the SP9 case is favorable to a strong expansion

in the spanwise direction while in the SP26 the axial velocity component is stronger. This may explain the low spanwise velocity in the SP26 configuration (Fig. 28(b), $t = 38.2$ ms).

To quantify the thrust effect in these two cases, a sample volume has been defined between the center axis of two successive injectors over the whole length of the combustion chamber (dashed lines in Fig. 28). The PDF of the spanwise velocity has been extracted from LES in this sample volume at $t = 26$ ms (SP9, Fig. 29(a)) and $t = 38.2$ ms (SP26, Fig. 29(b)), when the flame propagates through the sample volume. For comparison, the same PDF is extracted from an instantaneous isothermal LES solution for both cases in order to reveal the modifications induced by the flame. While both isothermal PDF are almost symmetrical and centered at a close to zero velocity in the spanwise direction, the reactive SP9 PDF clearly shifts toward positive spanwise velocity. On the contrary the reactive SP26 case PDF is a lot less modified as compared to its isothermal counterpart. It indicates the crucial role of expansion in traveling through initially (in isothermal conditions) low velocity LRZ.

5.4. Flow impact on the flame structure

The objective is now to focus on the flame response to the flow perturbations and equivalence ratio variations. Due to the rapid mixing induced by the swirled injection systems, the turbulent premixed combustion regime is dominant throughout the entire ignition sequences. Such flame consumption rate is sensitive to equivalence ratio fluctuations, curvature and stretch. In regions of highly perturbed flow the flame can be locally quenched, impacting its propagation.

The equivalence ratio is almost constant over the entire combustion chamber except in the vicinity of a burner, where the mixing time is reduced. In these region, the local heat release is increased because the premixed flame encounters higher

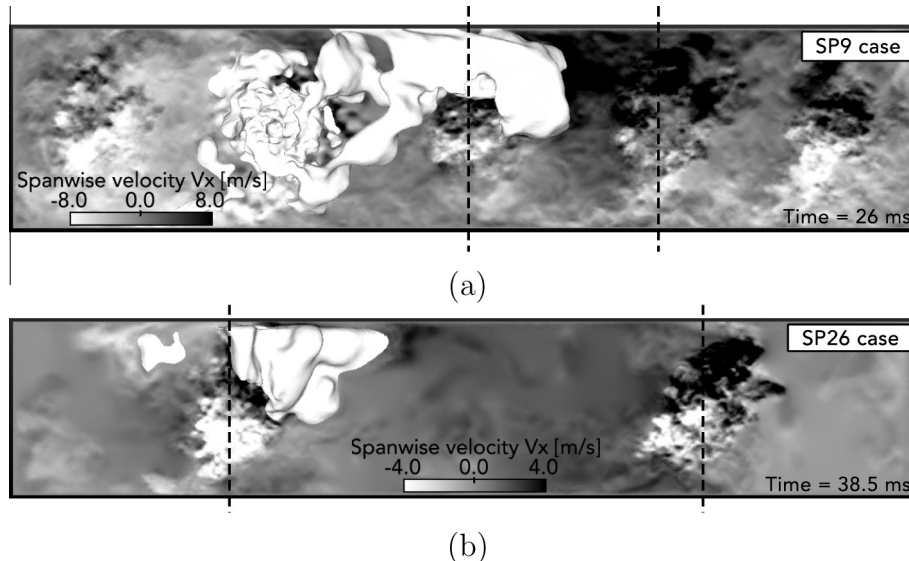


Fig. 28. LES results: thrust effects of burnt gas expansion for the SP9(a) and SP26(b) cases, respectively at $t = 26$ ms and $t = 38.2$ ms when the flame is between two successive injectors. Two Y-cut planes display the spanwise velocity at $z/D = 1.5$ (SP9) and $z/D = 2.5$ (SP26) and the propagating flame (white iso-surface of temperature), bottom view.

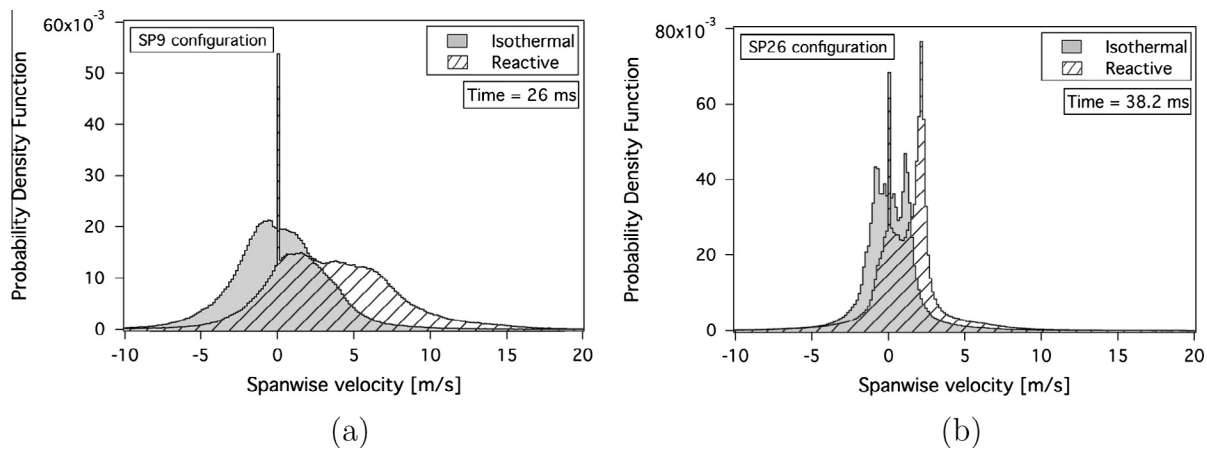


Fig. 29. LES results: PDF of the spanwise velocity in a restricted zone located between two successive injectors and identified in Fig. 28. PDF are obtained from reacting and non-reacting LES for the SP9 case at $t = 26$ ms (a) and the SP26 case at $t = 38.2$ ms (b).

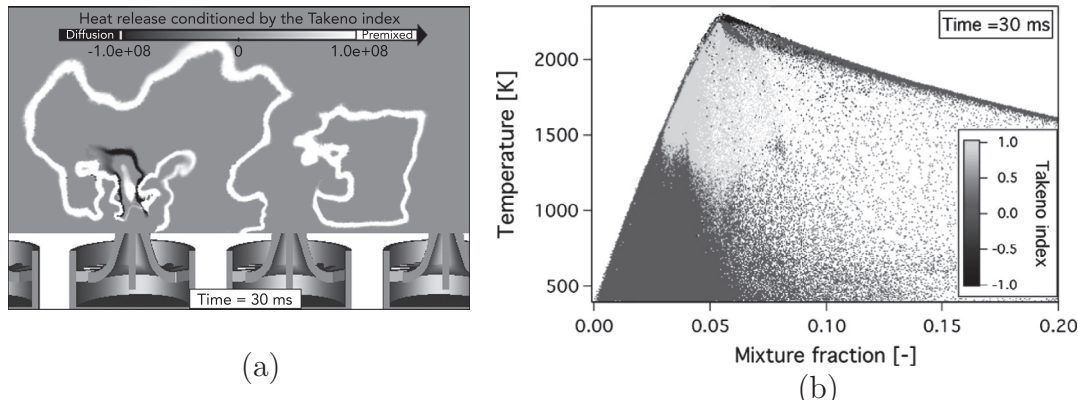


Fig. 30. LES results: (a) cut of heat release field conditioned by the Takeno index and (b) scatterplots of temperature as a function of the mixture fraction colored by the Takeno index (b), at $t = 30$ ms for the SP9 case. (For interpretation of the references to colour in this figure legend, the reader is referred to the web version of this article.)

equivalence ratios and higher turbulence. Locally the flame may be converted into a diffusion flame. This particular observation is

supported by Fig. 30(a) where the locally negative Takeno Index [38] evidences the presence of diffusion flames. Mixture

fraction/temperature scatterplots colored by the Takeno index (Fig. 30(b)) illustrate the wide range of equivalence ratios encountered, characteristic of partially premixed flames.

In the following the shear stress is used as an indicator of the flow disturbance applied to the flame front since it is a major part of flame stretch. The shear stress may be determined using the Tresca formula [39] as the difference between the maximum and the minimum of the eigenvalues of the stress tensor. PDFs of this shear stress at two instants are given in Fig. 31(a) and (b), respectively for the SP9 and SP26 configurations. The first instant is

chosen before the flame encounters the SWJ, while it keeps spreading in a quiet area where the flow shear stress is expected to be low ($t_1 = 6.5$ ms (SP9) and $t_1 = 21$ ms (SP26)). The second instant brings attention to a situation where part of the flame has been swept by the swirl motion and is subject to high turbulence in the SWJ ($t_2 = 16.5$ ms (SP9) and $t_2 = 38.2$ ms (SP26)). Figure 31 clearly shows much higher levels of stress applied to the flame in the SP9 case compared to the SP26 case, even prior to meeting the SWJ. It highlights the more perturbed velocity field in the SP9 case. As the flame reaches the SWJ, PDFs show very high shear

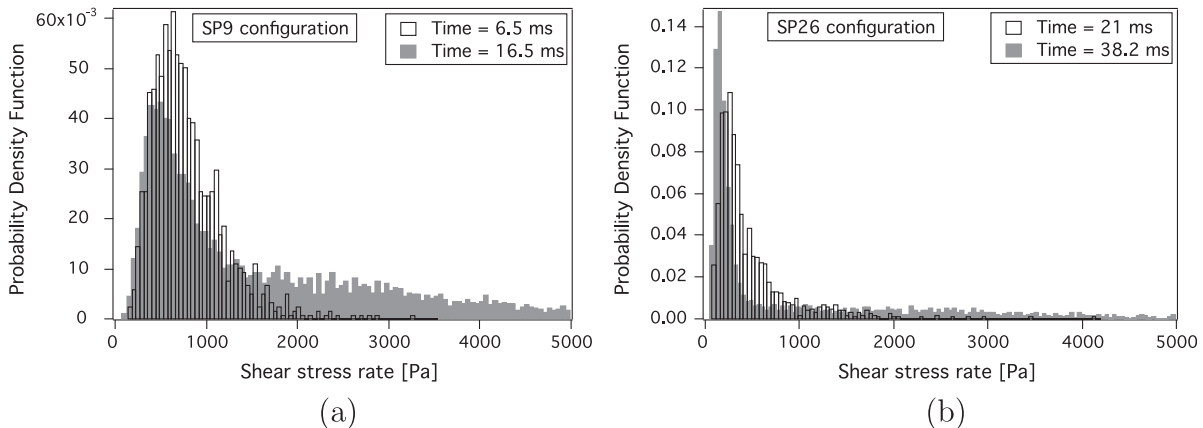


Fig. 31. LES results: PDF of the shear stress rate in the flame front (in the fresh gas side) at two different stages before and after the flame begins to reach the SWJ for the SP9 (a) and SP26 (b) configurations.

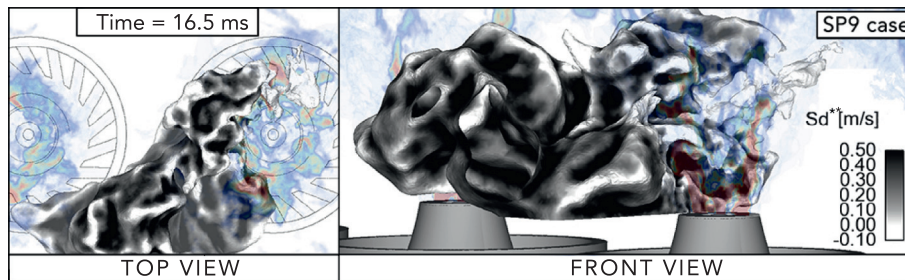


Fig. 32. LES results: visualization of an iso-surface at $c = 0.2$ colored by the flame front weighted displacement speed, case SP9, top view (left) and front view (right).

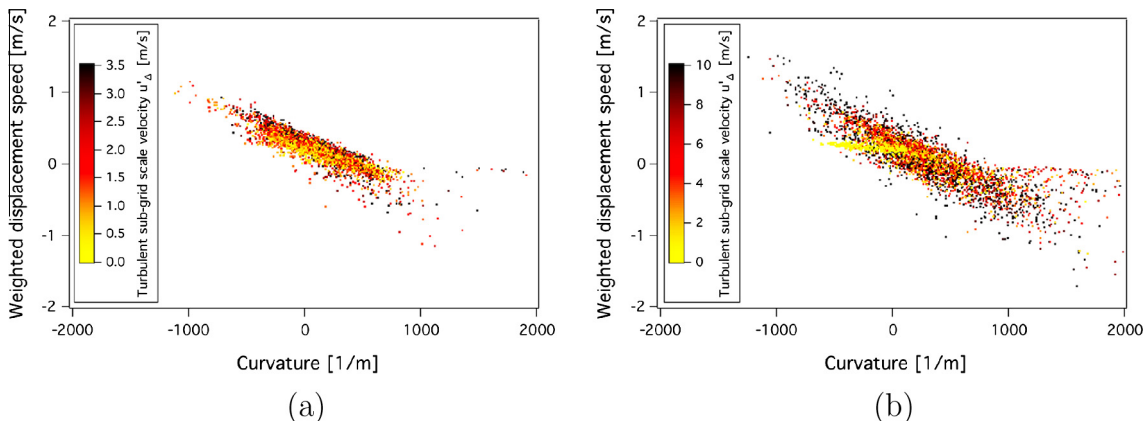


Fig. 33. LES results: scatterplot of the density-weighted displacement speed for the SP9 case at time $t = 16.5$ ms for low shear stress ($< 1000 \text{ Pa s}^{-1}$) (a) and high shear stress ($> 1000 \text{ Pa s}^{-1}$) regions (b), colored by the sub-grid velocity.

stress values susceptible to locally quench the flame, especially in the SP9 case (Fig. 31(a) $t_2 = 16.5$ ms).

In order to compare the displacement speed S_d to the laminar propagation speed S_L , the density variation has to be taken into account and the density-weighted displacement speed $S_d^* = \frac{\rho S_d}{\rho_f}$ is now preferred [40] where ρ and ρ_f correspond to the local and fresh gas densities respectively. As an illustration, Fig. 32 represents the flame front by the iso-surface $c = 0.2$ colored by its density-weighted displacement speed S_d^* for the SP9 case. Two distinct regimes are identified, in the inter-injector region and close to the SWJ respectively. The former is characterized by low shear stress (< 1000 Pa s $^{-1}$), where the flame displacement speed is mainly driven by flame surface wrinkling due to large scale turbulence, while the latter corresponds to high shear stress (> 1000 Pa s $^{-1}$) and small scale curvature. These different regimes are characterized in terms of S_d^* and curvature in Fig. 33 for SP9 case at the same time as Fig. 32. The color scale corresponds to the level of sub-grid turbulent velocity computed using the OP2 operator of Colin and Rudgyard [28]. As already found by Peters et al. [41], S_d globally follows a linear decrease with curvature. Lowest negative curvatures correspond to concave flames associated to positive S_d^* , while the highest positive curvature leads to thickened convex flames as revealed by the negative S_d^* [42]. Compared to the low shear region Fig. 33(a), the high shear stress region (Fig. 33(b)) shows a wider range of curvature and more spreading of S_d due to the higher level of sub-grid velocity. This leads to local flame quenching, resulting in a decrease of the total flame speed. This also explains the difficulty of the flame to penetrate in the SWJ and the increased traveling time to reach INJ1.

6. Conclusions and perspectives

Experiments and numerical simulation of ignition in a multi-injectors burner have been performed to study the effect of the distance between injectors on the ignition process and contribute to a better understanding of the mechanisms driving the light-around flame propagation. Comparisons between experiments and simulations and joint analysis provide valuable new information.

First, non-reacting cases have emphasized great differences on the main flow features at ignition time depending on the spacing between injectors. Modifications of the SWJ penetration and opening angle result in changes of the width and height of LRZ. The studied experimental set-up induces a reduction of the overall mass flow rate when the number of injectors decreases. The main consequence is a reduction of the swirl-induced circumferential motion.

Increasing spacing between consecutive injectors directly impact the flame propagation mode and thus the ignition delay. Two major propagation modes were identified both in LES and experiments. Small spacings (below 150 mm) allow a purely spanwise, rapid and safe propagation. A critical distance is identified (160 mm), above which propagation mechanisms begin to change. Above this limit, propagation occurs not only in the spanwise direction, but also in the axial direction. When this distance is further increased, flame propagation becomes mainly axial and full ignition is delayed or fails (seen only in the experiments).

A detailed analysis showed that the different propagation modes were essentially driven by two key mechanisms:

- The flame is affected by the flow aerodynamics which changes with the injector spacing. Low spacing flow aerodynamic promotes a rapid suction by the swirled motion leading to a spanwise flame propagation mode while high spacing flow structure changes are favorable to an axial propagation mode. The spanwise propagation mode is associated with short traveling time

of the flame from one injector to the other and a low variability while the axial propagation mode is characterized by longer propagation times and a much higher variability.

- A thrust effect due to the thermal expansion of the burnt gases has been highlighted. It produces a continuous flame progress which modifies the surrounding cold gas flow. It may increase the spanwise velocity and is the major mechanism of flame propagation in regions of weak mean flow such as LRZ.

These propagation modes result in different overall ignition times which increase with injector spacing. Comparisons between experiments and LES have shown the capability of LES to reproduce ignition sequences as well as the added value of LES in this investigation of ignition process thanks to the additional data available. Tools are now ready to study other ignition phenomena, such as the effects of liquid fuel injection or operating conditions. The application to annular burner and real combustor engines will allow to predict their ignition capability and will be crucial in the design process of such systems.

Acknowledgments

The research leading to these results has received funding from the European Community's Seventh Framework Program (FP7/2007–2013) under Grant Agreement No. ACP8-GA-2009-234009. This work was granted access to the HPC resources of [CCRT/IDRIS] under the allocation 2013-x20132b5031 made by GENCI (Grand Equipement National de Calcul Intensif). This research is also part of a 2013 INCITE award of the Department of Energy, it used resources of the Argonne Leadership Computing Facility at Argonne National Laboratory, which is supported by the Office of Science of the U.S. Department of Energy under contract DE-AC02-06CH11357.

References

- [1] A.H. Lefebvre, *Gas Turbine Combustion*, second ed., Taylor and Francis, 1998.
- [2] D. Bradley, C.G.W. Sheppard, I.M. Suardjaja, R. Woolley, *Combust. Flame* 138 (2004) 55–77.
- [3] A.P. Kelley, G. Jomaas, C.K. Law, *Combust. Flame* 156 (5) (2009) 1006–1013.
- [4] S. F Ahmed, E. Mastorakos, *Combust. Flame* 146 (2006) 215–231.
- [5] S.F. Ahmed, R. Balachandran, T. Marchione, E. Mastorakos, *Combust. Flame* 151 (2007) 366–385.
- [6] E. Mastorakos, *Prog. Energy Combust. Sci.* 35 (1) (2009) 57–97.
- [7] M. Cordier, A. Vandel, G. Cabot, B. Renou, A.M. Boukhalfa, *Combust. Sci. Technol.* 185 (3) (2013) 379–407.
- [8] A. Eysartier, B. Cuenot, L.Y.M. Gicquel, T. Poinsot, *Combust. Flame* 160 (7) (2013) 1191–1207.
- [9] A. Neophytou, E. Richardson, E. Mastorakos, *Combust. Flame* 159 (2012) 1503–1522.
- [10] M. Boileau, G. Staffelbach, B. Cuenot, T. Poinsot, C. Bérat, *Combust. Flame* 154 (1–2) (2008) 2–22.
- [11] W.P. Jones, A. Tylliszczak, *Flow Turbul. Combust.* 85 (2010) 711–734.
- [12] E. Bach, J. Kariuki, J.R. Dawson, E. Mastorakos, in: AIAA 51st Aerospace Science Meeting, Grapevine, Texas, January 2013.
- [13] J.-F. Bourguin, D. Durox, T. Schuller, J. Beaunier, S. Candel, *Combust. Flame* 160 (8) (2013) 1398–1413.
- [14] C. Schulz, V. Sick, *Prog. Energy Combust. Sci.* 31 (1) (2005) 75–121.
- [15] O. Degardin, B. Renou, A.M. Boukhalfa, *Exp. Fluids* V40 (3) (2006) 452–463.
- [16] M. Rudgyard, Integrated preprocessing tools for unstructured parallel CFD applications, Technical Report TR/CFD/95/08, CERFACS, 1995.
- [17] R.-H. Ni, *Am. Inst. Aeronaut. Astronaut. J.* 20 (1982) 1565–1571.
- [18] T. Poinsot, S. Lele, *J. Comput. Phys.* 101 (1) (1992) 104–129.
- [19] G. Lartigue, *Simulation Aux Grandes échelles de la Combustion Turbulente*, Ph.D. thesis, INP Toulouse, 2004.
- [20] V. Moureau, G. Lartigue, Y. Sommerer, C. Angelberger, O. Colin, T. Poinsot, *J. Comput. Phys.* 202 (2) (2005) 710–736.
- [21] O. Colin, M. Rudgyard, *J. Comput. Phys.* 162 (2) (2000) 338–371.
- [22] F. Ducros, F. Nicoud, T. Poinsot, in: Proceedings of 6th ICFD Conference on Numerical Methods for Fluid Dynamics, Baines MJ, 1998, pp. 293–300.
- [23] G. Lacaze, E. Richardson, T.J. Poinsot, *Combust. Flame* 156 (6) (2009) 1993–2009.
- [24] R. Maly, M. Vogel, in: 17th Symp. (Int.) on Combustion, The Combustion Institute, Pittsburgh, 1978, pp. 821–831.

- [25] G.F.W. Ziegler, E.P. Wagner, R.R. Maly, *Proc. Combust. Inst.* 20 (1985) 1817–1824.
- [26] Y. Ko, R.W. Anderson, V.S. Arpacı, *Combust. Flame* 83 (1991) 75–87.
- [27] B. Franzelli, E. Riber, L.Y.M. Gicquel, T.J. Poinsot, *Combust. Flame* 159 (2) (2012) 621–637.
- [28] O. Colin, F. Ducros, D. Veynante, T. Poinsot, *Phys. Fluids* 12 (7) (2000) 1843–1863.
- [29] J.-Ph. Léger, T. Poinsot, D. Veynante, in: Proc. of the Summer Program, Center for Turbulence Research, NASA Ames/Stanford Univ., 2000, pp. 157–168.
- [30] A.K. Gupta, D.G. Lilley, N. Syred, *Swirl Flows*, Abacus Press, 1984.
- [31] D. Barré, M. Kraushaar, G. Staffelbach, V. Moureau, L.Y.M. Gicquel, *Comp. Rend. Mécanique* 341 (1) (2013) 277–287.
- [32] N. Syred, *Prog. Energy Combust. Sci.* 32 (2) (2006) 93–161.
- [33] M. Cordier, A. Vandel, B. Renou, G. Cabot, M.A. Boukhalfa, M. Cazalens, in: ASME Turbo Expo 2013: Turbine Technical Conference and Exposition, 2013.
- [34] V. Subramanian, P. Domingo, L. Vervisch, Large eddy simulation of forced ignition of an annular bluff-body burner, *Combust. Flame* 157 (3) (2010) 579–601.
- [35] R.W. Read, J.W. Rogerson, S. Hochgreb, In: 46th AIAA Aerospace Sciences Meeting, Reno, Nevada, 7–10 January, 2008.
- [36] T. Marchione, S.F. Ahmed, E. Mastorakos, *Combust. Flame* 156 (2009) 166–180.
- [37] T. Poinsot, D. Veynante, *Theoretical and Numerical Combustion*, third ed., 2011. <<http://www.cerfacs.fr/elearning>>.
- [38] H. Yamashita, G. Kushida, T. Takeno, *Proc. R. Soc. Lond. A* 431 (1990) 301–314.
- [39] H. Tresca, *Acad. Sci. Paris* 2 (1) (1864) 59.
- [40] H.G. Im, J.H. Chen, *Combust. Flame* 119 (4) (1999) 436–454.
- [41] N. Peters, P. Terhoeven, J.H. Chen, T. Echekki, *Proc. Combust. Inst.* 27 (1998) 833–839.
- [42] N. Chakraborty, R.S. Mastorakos, E. Cant, *Combust. Sci. Technol.* 179 (1–3) (2007) 293–317.